A new 3D experimentally consistent XFEM to simulate delamination in FRP-reinforced concrete

Elena Benvenuti[1*], Nicola Orlando[1], Daniele Ferretti[2], Antonio Tralli[1]

[1] *ph. nr. +39 0532 974935 elena.benvenuti@unife.it, Dipartimento di Ingegneria, Università di Ferrara via Saragat 1, I-44122 Ferrara, Italy*

[2] *Dipartimento di Ingegneria Civile, dell'Ambiente, del Territorio e Architettura DICATeA, Parco Area delle Scienze, 181/A, daniele.ferretti@unipr.it +39 0521 905943*

Abstract

FRP-based reinforcements are increasingly used for the structural rehabilitation of buildings damaged by seismic loadings. Single-lap shear tests on FRP-reinforced concrete blocks are often performed to assess the maximum transferable load before delamination. In this paper, an effective 3D regularized extended finite element model (XFEM) is proposed to study single-lap shear tests. The bending of the FRP plate, the influence of FRP plate width, and the two-way delamination for variable bonding length are assessed. Based on a suitable choice of the level sets associated with the XFEM enrichment, the proposed model can be used for design purposes besides, or in alternative to, experimental tests.

Keywords: A: 3-Dimensional reinforcement, B: delamination, C: Finite element analysis (FEA), C: Computational modelling, XFEM

1. INTRODUCTION

Fiber Reinforced Polymers (FRP) reinforcements are increasingly used for the post-seismic structural rehabilitation and to enhance the ultimate strength of concrete structural elements. Single-lap shear tests on FRP-reinforced concrete blocks are often performed to assess the ultimate load before the complete delamination of the FRP plate [1] occurs. Delamination is a complex three-dimensional (3D) process, and a challenging issue in computational mechanics [2, 3]. To study single-lap shear tests, we present an effective eXtended

Finite Element Model (XFEM) based on an experimentally consistent level set system. Key aspects, such as the peeling and the bending of the FRP plate and the influence of the FRP plate length and width, are investigated.

Based on experimental results, it is known that the delamination process involves a thin portion of material localized in the concrete layer underlying the FRP plate. Within finite element (FE) approaches, the concrete block is commonly modeled as a two-dimensional (2D) body in plane stress state, and the FRP-concrete interface as a one-dimensional interface subjected to distributed tangential stress by means of bond stress-slip laws [4, 5]. However, even if the reinforcement is loaded mainly in shear, the out-of-plane displacements observed during the tests induce tensile and compression stresses orthogonal to the bonding plane [6]. Hence, one-dimensional bond stress-slip relationships have been modified to take into account failure mechanisms relying on mixed fracture modes [7, 8]. Furthermore, experimental tests [9, 10] detected the occurrence of edge regions with high shear strains associated with the stress transfer from FRP to concrete, and highlighted the key role of the peel displacement in the delamination onset and propagation. In particular, a two-way debonding mechanism was observed [6]. For very short bonding lengths, debonding starts at the free end of the FRP plate and propagates towards the loaded end of the plate. For sufficiently long bonding lengths, debonding starts at the loaded end and propagates towards the free end until a critical bonding length is reached, at which delamination at the free end starts and propagates towards the loaded end. Furthermore, the maximum transferable load is influenced by the FRP plate bending, and the ratio between the widths of the plate and the concrete block.

Width-effects associated with shear-strain-edge-regions cannot be taken into account assuming a plane stress state. For this reason, 3D FE codes [12] have been used, most of them assuming the concrete-FRP surface as a zero thickness interface. Based on this assumptions, 3D FE simulations highlighted the dependence of the concrete stress state on the bending rigidity of the FRP plate and the edge stiffening effect on the shear stress components. To this purpose, the analysis in reference [11] assumed elastic materials, and a perfect bond between the adhesive and the FRP plate. An elastic-damage interface model governing the interlaminar stresses acting in the sliding direction was adopted in a more recent study [12]. Furthermore, based on a bond stress-slip law, Neto et al. [13] have introduced an effective bond width that comprehends of both the FRP plate and the contiguous concrete with

non-vanishing shear stress.

Delamination in composite laminates has been effectively simulated through the XFEM [14], a partition of unity FE method proposed by Belytschko and coworkers [15]. This method incorporates features of the expected solution at the nodal level. Unlike standard FE models, the XFEM makes it possible to adopt meshes, that are independent of the geometry of cracks and interfaces. In the XFEM, interfaces are usually introduced in an implicit way as level set functions [16]. Applications of the XFEM are really wide. For instance, the XFEM was exploited to simulate fracture of composite laminates [2], and the damage progression in laminated overheight compact tension specimens using representations of individual cracks [17], or by means of an XFEM formulation based on a discrete damage zone model [18]. The phantom-node method, a variation to the XFEM, has been used for a mesh-independent 3D representation of matrix cracks as straight discontinuities in the displacement field [19]. While the use of the XFEM for the 3D modelling of delamination in composite laminates is quite established, 3D XFEM simulations of pull-out tests of FRP plates bonded to concrete specimens seem not to have been presented in the literature.

We propose here an original 3D regularized version of the XFEM method with a global-local level set system that is able to take into account edge effects. This regularized XFEM approach was previously developed by the Authors for 2D plane-stress simulation of delamination [20] to study, for instance, the transition from strain localization to crack [21], and inclusions with imperfect interfaces [22]. In particular, the delamination strength was predicted with a sufficient accuracy exploiting just the nominal values of the Young moduli and the Poisson coefficients of concrete, glue, and reinforcement. The robust continuous-discontinuous transition ensured mesh-size independent, energy-consistent structural results, and avoided the sudden loss of stiffness that frequently occurs with other continuous-discontinuous procedures [23]. While complex interface damage laws have been proposed in the literature [24, 25], in the regularized XFEM approach to delamination [20], the damage evolution was associated with both shearing and normal opening through a simple Rankine-type law. Very reliable results and an excellent agreement with the experimental results were reached.

With respect to the previous 2D model [20], the 3D regularized XFEM formulation proposed herein is characterized by a global-local system of level sets taking into account the edge effects and a fully 3D mixed shearing-peeling debonding mechanism. The main

aim of this contribution is not only to fit the experimental results, that are often subjected to several uncertainties, but also to provide a reliable technical tool that can be used for design purposes besides, or in alternative to, experimental tests.

After a basic introduction to the computational model in Sec. 2, the results obtained for the data sets [6] and [26] are shown in Sec. 3. Emphasis is put on the bending of the FRP plate, the presence of the peeling displacements at both the loaded and the free ends of the FRP plate, and the two-way delamination depending on the bonding length. The 3D behavior of the delamination process is assessed in Sec. 4, where the width dependence of the maximum transferable load is also displayed.

2. Introduction to the computational model

To model correctly the delamination process, an effective computational formulation has to: i) tackle the possible mesh-size dependency induced by the adoption of a softening constitutive law for concrete; ii) ensure a smooth continuous-discontinuous transition where delamination occurs; iii) reproduce the 3D debonding of the FRP plate taking into account the edge effects. In previous studies, we have proved that the regularized XFEM approach satisfies the mesh-independency requirement [22, 21], and ensures a smooth continuous-discontinuous transition [21]. Hereinafter, only the aspects related to the 3D debonding of the FRP plate taking into account the edge effects will be assessed. Sec. 2.1 focuses on the general aspects of the regularized XFEM approach, such as the regularized kinematics, and a smooth mechanically-consistent continuous-discontinuous-transition procedure. 3D modelling of delamination of FRP plates from concrete blocks requires a specific strategy different from that adopted to study 2D delamination, as discussed in Sec. 2.2.

2.1. Kinematics, constitutive laws and continuous-discontinuous computational procedure in the regularized XFEM

Let the displacement field $\mathbf{u}$ be discontinuous across the delamination surface $\mathcal{S} \in \mathbb{R}^3$ of normal $\mathbf{n}_S$. Within a single element of nodal degrees of freedom $\mathbf{U}^e$ and $\mathbf{A}^e$ interpolated by the usual FE interpolation functions $\mathbf{N}^e$, the regularized XFEM displacement $\mathbf{u}^e$ of element e is [15]

$$\mathbf{u}^e = \mathbf{N}^e\mathbf{U}^e + \mathcal{H}_\rho\mathbf{N}^e\mathbf{A}^e\,, \tag{1}$$

where $\mathcal{H}_\rho$ is a regularized Heaviside function that approximates the Heaviside function for vanishing regularization length ρ. The vector $\mathbf{A}^e$ collects the jump components along x, y and z for the finite element e. $\mathcal{H}_\rho$ is assumed a function of the distance from the *global* level set plane. By compatibility, the strain field is

$$\boldsymbol{\varepsilon}^e = \mathbf{B}^e\mathbf{U} + \mathcal{H}_\rho\mathbf{B}^e\mathbf{A}^e + \|\nabla\mathcal{H}_\rho\|(\mathbf{N}^e\mathbf{A}^e \otimes \mathbf{n}^e)\,, \tag{2}$$

where $\mathbf{B}^e = \nabla\mathbf{N}^e$ is the standard FE compatibility matrix. Usually, $\mathbf{n}^e$ denotes the vector normal to the surface across which the displacement field exhibits a discontinuity [15]. In our approach, we start from the experimental evidence [6] that the crack orientation in the concrete below the FRP plate is variable in the space, namely it is different at the boundaries of the detachment surface and within the detachment surface (Fig. 2). Therefore, $\mathbf{n}^e$ is assumed to change from element to element according to a *local level set* attached to each Gauss point, as described in Sec. 2.2.

FRP and adhesive are modelled as linear elastic materials. At each Gauss point, we introduce the damage variables D and D_c for the concrete and the zone where debonding occurs, respectively, and compute the associated stresses thorough

$$\boldsymbol{\sigma}^e = (1-D)\mathbf{E}\,\mathbf{B}^e\mathbf{U} + \mathcal{H}_\rho\,(1-D)\mathbf{E}\,\mathbf{B}^e\mathbf{A}^e\,, \tag{3a}$$

$$\boldsymbol{\sigma}_c^e = (1-D_c)\mathbf{E}_c\|\nabla\mathcal{H}_\rho\|(\mathbf{N}^e\mathbf{A}^e \otimes \mathbf{n}^e)\,. \tag{3b}$$

Note that the stress $\boldsymbol{\sigma}_c^e$ (3b) is computed taking into account the *local level set system* described in Sec. 2.2. In particular, the concrete damage is governed by an exponential Rankine elasto-damaging law until D has reached the critical value D^{cr} [22]. As soon as $D \geq D^{cr}$, the evolution of D is dropped, i.e. the concrete can only elastically unload: a regularization zone replaces the discontinuity. In particular, the damage evolution can be D_c affecting the stress $\mathbf{t}$ is

$$D = \min\{D^{cr}, f(r)\}\,, \quad D_c = \max\{D^{cr}, f(r)\}\,, \quad f(r) = 1 - \frac{r_0}{r_c}\exp\!\big(-2\,H\frac{r_c - r_0}{r_0}\big)\,, \tag{4}$$

where $r_c \geq r_0$, with $r_0 = f_t$ for tensile damage, and $r_0 = f_c$ for compressive damage. For a monotonic damage process in a one-dimensional bar the stress-strain law obeying Eq. (4) is shown in Fig. 1 for $H = 0.008$ MPa (blue continuous line) and $H = 0.005$ MPa (red dotted

line) with fixed $f_t = 3.21$ MPa.

The main differences between the proposed regularized XFEM procedure and standard applications of the XFEM are synthesized in Tab. (1). In particular, the standard elemental stiffness $\mathbf{K}^e_{st}$ is

$$\mathbf{K}^e_{st} = \begin{bmatrix} \mathbf{B}^{e\,t}\,(1-D)\mathbf{E}\,B_u & \mathbf{B}^{e\,t}\,(1-D)\mathbf{E}\,\nabla(\mathcal{H}_\rho\mathbf{N}^e) \\ \nabla(\mathcal{H}_\rho\mathbf{N}^e)^t(1-D)\mathbf{E}\mathbf{B}^e & \nabla(\mathcal{H}_\rho\mathbf{N}^e)^t\,(1-D)\mathbf{E}\nabla(\mathcal{H}_\rho\mathbf{N}^e) \end{bmatrix}, \tag{5}$$

with $\nabla(\mathcal{H}_\rho\mathbf{N}^e) = \mathcal{H}_\rho\,\mathbf{B}^e + \nabla\mathcal{H}_\rho \otimes \mathbf{N}^e$. The adopted stiffness matrix is

$$\mathbf{K}^e_{reg} = \begin{bmatrix} \mathbf{B}^{e\,t}\,(1-D)\mathbf{E}\,B_u & \mathbf{B}^{e\,t}\,\mathcal{H}_\rho(1-D)\mathbf{E}\,\mathbf{B}^e \\ \mathbf{B}^{e\,t}\,\mathcal{H}_\rho(1-D)\mathbf{E}\,\mathbf{B}^e & \mathbf{B}^{e\,t}\,\mathcal{H}^2_\rho(1-D)\mathbf{E}\mathbf{B}^e + \|\nabla\mathcal{H}_\rho\|\bar{\mathbf{N}}^{e\,t}(1-D_c)\mathbf{E}_c\bar{\mathbf{N}}^e \end{bmatrix}, \tag{6}$$

where the operator $\bar{\mathbf{N}}^e$ is such that $\nabla\mathcal{H}_\rho \otimes \mathbf{N}^e A \approx \|\nabla\mathcal{H}_\rho\|\bar{\mathbf{N}}^e\mathbf{A}_e$. The differences between the stiffness matrices (5) and (6) stem from the adopted variational formulation, which has been thoroughly described in [28, 27].

2.2. Definition of the fracture process zone based on global-local level set system

In the studied pull out tests, a concrete layer like that shown in Fig. 2 remains attached to the delaminated FRP plate [6], being thicker at the ends of the bonded zone, and in correspondence with large concrete aggregates. In this case, a shear process zone with cracks orthogonal to the maximum principal stress, thus inclined with respect to the adhesive surface, is often assumed [29]. In the previous applications of the regularized XFEM approach, a unique global level set was defined representing, for instance, the implicit surface of the inclusion in the study of particulate composites [28], or the crack path in strain localization problems [22, 21]. The normal vector $\mathbf{n}$ coincided with the geometric normal to the interface surrounding the inclusion. In the present study, a different level set system is adopted, called *global-local level set* system. This is the main original aspect of the adopted approach with respect to the previous applications of the regularized XFEM approach. In this study, delamination is assumed to take place in a plane parallel to the adhesive layer, as usual in the literature [5, 3]. Such a plane has been located at 1 mm underneath the concrete surface. This corresponds to confine the delamination process in the finite element layer placed immediately below the glue. The hypothesis agrees with the experimental evidences in the central part of the plate (Fig. 2), where a layer of concrete 1 to 3 mm thick is usually

detached [6]. Of course, the concrete bulbs at the ends of the bonded zone are not caught.

The *global-local level set* procedure relies in the fact that we assume: a *global* level set function denoting the surface of the delamination that is parallel to the adhesive surface and located below the concrete surface, and a *local* level set system at each Gauss point of the XFEM enriched finite elements, displayed in Fig. 3. The global level set surface is defined a priori parallel to the adhesive layer, as usual in two-dimensional FE analysis and in numerical models based on one-dimensional interface laws.

As for the *local* level set system, we have adopted the following path of reasoning. In principle, the $\mathbf{n}^e$ vector in the constitutive equation (3b) is orthogonal to the crack direction and governed by the maximum tensile principal stress. This means that the computation of the principal stresses has to be performed at each of the Gauss points for each equilibrium iteration per each enriched finite elements. Therefore, hundreds of equilibrium iteration are sometimes required to get convergence, the resulting computational procedure would turn out being rather CPU demanding. Instead of proceeding in this way, in this study, we have adopted the simplified *local* level set shown in Fig. 3. Each edge is associated with a local set whose normal vectors are shown in red and blue. The blue normals are oriented at $(0, 0, -1)$ for $x > 0$, $y > 0$, $z > 0$. The red normals are oriented outwards the edges along the direction $(1/\sqrt{3}, 1/\sqrt{3}, -1/\sqrt{3})$ for $x > 0$, $y > 0$, $z > 0$. The local level set adopted inside the enriched layer is associated with a normal field, plotted in green in the same figure, oriented towards the symmetry plane $y - z$ at $(-1/\sqrt{3}, 1/\sqrt{3}, -1/\sqrt{3})$ for $x > 0$, $y > 0$, $z > 0$, $\mathbf{n}$ being specular with respect to the $y-z$ plane in the domain $x < 0$, $y > 0$, $z > 0$. This assumption ensures that the delamination process is captured consistently. Noteworthy, the adopted *global-local level set* system is imposed a priori, but the final directions of the jump vectors $\mathbf{A}^e$ at the nodes are computed by the nonlinear iterative-incremental procedure and will not generally coincide with that of the superimposed normals. Moreover, the enriched layer of elements has the same width as the FRP plate, and is located 1 mm below the adhesive layer.

3. FRP plate bending, peeling and twofold delamination onset

This section is devoted to the study of the influence of the FRP plate bending and illustrates the occurrence of peeling at both the ends of the FRP plate depending on the bonding length. The values of the Young modulus and the Poisson coefficient adopted for

the FRP plate, the glue, and the concrete used in the model are collected in Tab. 2 as indicated in the references of the experimental works.

The regularized XFEM code used in this paper is a development of a Fortran 3D code for elastic materials and standard XFEM [28].

After an introduction to the geometry and material properties in Sec. 3.1, Secs. 3.2 and 3.3 analyze the strain in the concrete substrate, the peeling. Moreover, the forthcoming sections investigate the influence of the bonding length and the width of the FRP plate on both the structural response and the delamination activation.

3.1. Experimental tests geometry

For a comparison with experimental results, we will consider the experimental campaign of Chajes et al. [26], often studied in the literature, and the tests by Carrara et al. [6]. It is remarkable that, while for the former data set the structural response has been recorded up to the maximum load, for the latter data set, the whole load-displacement curves with softening post-peak branches have been recorded, owing to a stable loading control procedure developed for this purpose. All the data of the geometry and the material parameters of the original tests are collected in Tab. 2. In the geometry adopted by Chajes et al. [26] shown in Fig. 4a, the glue layer starts at the front of the specimen, namely close to the loaded end of the FRP plate. On the contrary, in the geometry of Carrara et al. [6], shown in Fig. 4b, the FRP plate is bonded at a certain distance from the front of the specimen to avoid the detachment of a concrete wedge when pulling the FRP plate. Moreover, the softening modulus H has been set equal to 0.005 MPa for the Chajes et al. [26] test, and equal to 0.008 MPa for the Carrara et al. [6] test.

Based on symmetry reasons, only one half of the specimen has been meshed. Considering that the concrete block stiffness plays an important role on the structural response of the specimen, we have first run some simulations where the real dimensions of the concrete block were modeled. Then, to reduce the computational burden, we have run the same simulations but with a width of the meshed geometry of the concrete block equal to 80 mm. These simulations gave the same results of the case with the entire width of the concrete block. Also the height of the concrete block has been taken equal to 35 mm to reduce the computational effort. These results seem to be confirmed also in [31]. The mesh adopted for Chajes et al. [26] in the $L_b = 101.6$ mm case shown in Fig. 5 is made of 250548 elements with 243930 total degrees of freedom.

3.2. Structural response, delamination onset and propagation

As the complete data set of Carrara et al. [6] test is available up to the final delamination stage is available, the corresponding delamination process has been assessed for various bonding lengths.

To compare the computed structural responses with the experimental ones, we have plotted the load vs both the z displacement u_1 at the loaded end and the z displacement u_2 at the free end of the FRP plate. Different bonding lengths L_b have been considered, from the short length $L_b = 30$ mm shown in Fig. 6a, to the longer lengths $L_b = 90$ mm and $L_b = 120$ mm, displayed in Figs. 6b and 6c, respectively. The snap-back in the structural response plotted in terms of the front-displacement increases as the bonding length increases, as shown in the case of $L_b = 90$ mm in Fig. 6b, and in the case of $L_b = 120$ mm in Fig. 6c.

The maximum transferable loads computed with the present analysis are shown for variable bonding length in Fig. 7a. In addition to the previous load-displacement simulations, the structural responses up to the maximum transferable load have been determined for the Chajes et al. [26] geometry too. For this latter case, the maximum transferable loads vs the bonding length are shown in Fig. 7b.

The different types of structural behavior for the Carrara et al. [6] tests shown in Fig. 6 are associated with different positions of the delamination onset. Because the detachment is strictly related to the evolution of the damage variable D_c, it is thus convenient to consider the evolution of D_c, which is the damage on the concrete surface below the glue. Figs. 8 display the sequence of the contour plots of D_c for $L_b = 30$ mm and $L_b = 90$ mm at the pre-peak, the peak and the post-peak loads, from top to bottom. In the case of short bonding length, $L_b = 30$ mm, damage starts at the free end. On the contrary, for the $L_b = 90$ mm case displayed in Fig. 8b, the damage evolution is different, as shown in Fig. 9 for the pre-peak, peak and post-peak stages. In a first stage, the damage develops at both the loaded and the free end of the FRP plate (a, b), it subsequently propagates from the loaded end towards the free end (c) up to a certain value of the actual bonded length, approximately equal to 30 mm (d), then it propagates from the free to the loaded end (e) up to complete delamination (f). An animation of the damage propagation for the $L_b = 90$ mm case is also shown in the supplementary file.

For all the investigated bonding lengths, the bending of the FRP plate influences the damage onset and its evolution. Such an influence is shown in Fig. 10 for the Chajes et

al. [26] test with bonding length $L_b = 50.8$ mm. The same figure shows that, for this bonding length, delamination proceeds from the free end to the loaded end of the FRP plate.

To complete the picture of the 3D delamination process, the tangential stress τ_{yz} and the peel stress σ_{yy} have been evaluated at the Gauss points on the concrete surface below the glue for the Carrara et al. [6] test. Figs. 11 display the spatial frames of σ_{yy} and τ_{yz} stress components, on the left and on the right column, respectively, detected at the pre-peak, the peak and the post-peak for the $L_b = 90$ mm case. In particular, in a first stage, the peel stress σ_{yy} is activated at the loaded end (a) and subsequently at the free end (b, c, d). In the final stages (e, f), peeling at the loaded end is predominant. The shearing stress τ_{yz} first propagates from the loaded end to the free end (a,b), then its peak moves from the free to the loaded end (c, d, e). Moreover, the shear stress τ_{yz} evaluated at the end of the FRP plate reaches values of 15 MPa, which are slightly high with respect to the experimental ones. The profile of τ_{yz} cannot be directly compared to the "shear stress" of one-dimensional shear-stress-slip laws [5], which are average values obtained from the variation of two subsequent strains measured by strain gauges on the plate surface. For instance, an example of shear-stress-slip law equivalent to the experimental one was deduced from the results obtained by means of the regularized XFEM approach in the 2D case [20].

3.3. Strain evolution and deformability

The strain evolution for various load levels have been compared with the available experimental results for both the experimental data sets. For this purpose, we have obtained from our 3D results a shear strain equivalent to that usually obtained in experiments from the displacements recorded at the strain gauges. In particular, the expression $\varepsilon = (u_{z,i+1} - u_{z,i})/\Delta z_i$, has been exploited, where z is the longitudinal axis, and $u_{z,i+1}$ and $u_{z,i}$ denote the displacements recorded on the FRP plate at discrete positions z_i and $z_{i+1} = z_i + \Delta z_i$. In Fig. 12, the evolution of the strain along the z-axis is shown for the Chajes et al. [26] tests at the maximum transferrable load. The post-peak strain profiles have not been reported, because the experimental post-peak data are not available. Profiles of the same colors correspond to the same load level, while the markers indicate the experimental results. For the Carrara et al. [6] experimental data, the strain profiles corresponding to both the pre-peak and the post-peak branches are available. In Fig. 13 the strain profiles

computed for the two bonding lengths $L_b = 90$ mm and $L_b = 120$ mm are compared with the homologous experimental profiles.

A good agreement between numerical values and tests is confirmed for both the experimental campaigns.

4. 3D aspects: Width and edge effects

To highlight the 3D aspects of delamination, this section investigates the profiles of several relevant stress components along the width and the length of the FRP-plate. In Sec. 4.1, the influence of the FRP plate width on the structural response is assessed. For this purpose, the Chajes et al. [26] tests are taken into account. In Sec. 4.2, the main results obtained for the cases investigated, are discussed.

4.1. Influence of the FRP plate width

The delamination analysis has been performed for variable FRP plate widths b. For $b/B > 0.5$, the width of the concrete is insufficient to allow a full transmission of the stresses from the FRP plate to the concrete substrate [10]. Therefore, the concrete width of the specimen analyzed has been set equal to 80 mm. In particular, the peel stress σ_{yy} and the shearing stress τ_{yz} have been plotted at the Gauss points of the finite elements within the bonded concrete. They are displayed in Fig. 14 for two widths of the FRP plate, namely $b = 15$ mm and $b = 45$ mm for the same bonding length $L_b = 101.6$ mm. The profiles have been detected at the peak of the transferable load. Fig. 14 display no appreciable edge effect for both the values of b.

The profiles of the shearing and the axial strain components ε_{xz} and ε_{zz}, respectively, have been plotted across the width at different locations along the FRP plate length for b=15 mm, b=45 mm, and $L_b = 101.6$ mm. Figs. 15 show the values detected during the elastic stage, before that the delamination process starts, while Figs. 16 display the evolution of these specific strain components during the delamination process. The profiles correspond to $z = 0.5$ mm (cyan dotted line), $z = 18.1$ mm (pink dashed line), $z = 38.1$ mm (yellow dash-dotted line), $z = 58.1$ mm (green dotted line), $z = 78.1$ mm (red dashed line) and $z = 95.1$ mm (blu continuous line). During the elastic stage, the profiles of ε_{xz} and ε_{zz} extend over a region significantly larger than b (Fig. 15). This confirms that the modelled concrete support must be sufficiently large compared to the FRP plate width to allow a

full diffusion of the shearing stress components in the concrete surrounding the FRP plate, as observed by Subramaniam et al. [10]. While ε_{zz} at the center of the FRP plate are almost constant, ε_{xz} is antisymmetric with respect to the symmetry plane. Both of them display high variations over an edge region approximately 20 mm wide. When the load reaches 90% of the peak load, the damage has been activated at the edges of the concrete substrate underlying the FRP plate. Correspondingly, the ε_{xz} and ε_{zz} shown in Fig. 16 display narrower edge regions of width approximately equal to 10 mm, in agreement with the experimental results reported in [6].

Furthermore, the dependence of the strain profiles on the bonding length has been assessed. Figs. 17 and 18 display the strain components during the elastic stage and at the peak, respectively, for the bonding lengths $L_b = 152.4$ mm and $L_b = 202.3$ mm. These bonding lengths are close to the asymptotic value predicted by Fig. 7b. The strain profiles have been evaluated at a distance from the front of the concrete block of 25.4 mm (blue line), 50.8 mm (red line), and 76.2 mm (green line). The results show that the strain diffusion in the concrete surrounding the FRP is substantially independently of L_b.

The widths of the edge regions computed through the present model are smaller than those experimentally detected by Subramaniam et al. [10], who measured edge regions approximately 20 mm wide for both ε_{xz} and ε_{zz}. Analogously to Subramaniam et al. [10], the width of the edge regions measured in this study is independent of b. These widths have not been imposed, and have been observed after post-processing the results. Indeed, the enriched layer of elements where the debonding is simulated has a width equal to that of the FRP plate.

In Fig. 19a, the dependence of the maximum stress $\sigma_u = P/(b\,t_f)$ transferable through the FRP plate width is displayed. The same figure displays the results obtained with the CNR-design formula [32]

$$\mathrm{P}_{max} = b_f \sqrt{2\,E_f\,t_f\,\Gamma_F} \tag{7}$$

where Γ_F is the specific fracture energy formulated as

$$\Gamma_F = k_b\,k_G\,\sqrt{f_{cm}\,f_{ctm}} \tag{8}$$

where $k_b = \sqrt{\frac{2-b_f/b}{1+b_f/b}} \geq 1$ for $b_f/b \geq 0.25$, and $k_b = 1.1832$ for $b_f/b < 0.25$, and k_g is usually taken in a range going from to 0.063 for preformed composites to 0.077 for in situ impreg-

nated composites. The results of our simulations are perfectly fitted by the CNR rule (7) using $k_b = 1.1832$ and $k_g = 0.065$, and the nominal properties of the concrete and the FRP that are, f_{cm}=43 MPa, f_{ctm}=3.21 MPa and t_f=1 mm, L_b=101.6 mm, E_f=108380 MPa.

4.2. Discussion

The agreement with the CNR rule [32] shown in Fig. 19a confirms that the developed computational model is a reliable design tool. The computed trend of the maximum transmissible stress shown in Fig. 19a is decreasing with increasing FRP plate width b and tends to an asymptote for large widths. On the contrary, based on their experimental tests, where the concrete widths B equal to 52 mm and to 125 mm were taken, Subramaniam et al. [9, 10] concluded that, below the critical value 0.5 of the ratio b/B, the maximum transmissible stress increases for increasing width of the concrete support. On the other hand, Fig. 19b shows that the maximum transferable load increases with the width b. We have investigated also larger widths B, but the same decreasing trend has been found. A more extensive numerical campaign is necessary to understand whether larger ratios b/B, namely larger concrete supports, may correspond to an increasing ultimate stress for increasing b. Furthermore, the occurrence of peel stress can potentially affect the results for relatively small bonding lengths, such as in the current case. To summarize, the results presented in Sec. 4 have shown that:

- Where the FRP plate is still attached to the concrete substrate, the profiles of the strain components ε_{xz} and ε_{zz} along the length of the FRP plate are not uniform across the width, and display high gradients localized at edge regions of the FRP plate comprehensive of both the FRP plate edges and the surrounding concrete.
- Where delamination has been activated, the edge regions, intended as the regions with high gradients, corresponding to the ε_{xz} and ε_{zz} profiles are localized in a narrower zone.
- The edge regions corresponding to the ε_{xz} and ε_{zz} profiles have a width independent of b and L_b.
- For the investigated geometries, the maximum transferable load increases for increasing width b of the FRP plate.
- For the assumed b/B ratios, the maximum load increases while the maximum stress transmissible through the FRP plate slightly decreases with the width in agreement

with the CNR-rules [32].

5. CONCLUSIONS

A regularized XFEM approach with an experimentally consistent level set system has been proposed for single-lap shear tests. It has been shown that: i) the bending of the FRP plate plays a remarkable role on the debonding of the FRP plate; ii) an edge strengthening effect due to the shear strain localization occurs along the edges of the FRP plate; iii) the common design rules prescribing the variation of the nominal maximum stress with the bonded width of the FRP plates have been confirmed; iv) a two-way delamination can be observed.

As for the question whether a 3D or a 2D analysis should be preferred, the obtained results have shown that, while the strain profiles along the FRP plate length, the peeling and the different delamination onset locations can be detected indifferently through 3D and 2D analyses, the shear and axial strain on the debonded concrete surface display an edge effect that can be captured only by means of a 3D analysis. Moreover, the dependence of the maximum transferable load on the bonding width can be assessed only through a 3D analysis.

Finally, the proposed regularized XFEM approach fits, and can be used as an alternative to, experimental tests.

Acknowledgements: The Authors gratefully acknowledge Prof. Giulio Ventura for having allowed them to use his workstation.

References

[1] B. Taljsten, Strengthening of concrete prisms using the plate bonding technique, International Journal of Fracture 82 (1996) 253–266.

[2] SE. Ashari, S. Mohammadi, Delamination analysis of composites by new orthotropic bimaterial extended finite element method, International Journal for Numerical Methods in Engineering 86 (2011) 1507–1543.

[3] L. De Lorenzis, Some recent results and open issues on interface modeling in civil engineering structures, Materials and Structures 45 (2012) 477–503.

[4] L. De Lorenzis, A. Nanni, Bond of FRP laminates to concrete, ACI Materials Journal 98 (2001) 256–264.

[5] B. Ferracuti, M. Savoia, C. Mazzotti, Interface law for FRP-concrete delamination, Comp. Struct. 80 (2007) 523–531.

[6] P. Carrara, D. Ferretti, F. Freddi, G. Rosati, Shear tests of carbon fiber plates bonded to concrete with control of snap-back, Engineering Fracture Mechanics 15 (2011) 2663–2678.

[7] E. Martinelli, C. Czaderski, M. Motavalli, Modeling in-plane and out-of-plane displacement fields in pull-off tests on {FRP} strips, Engineering Structures 33 (2011) 3715–3725.

[8] P. Carrara, D. Ferretti, A finite-difference model with mixed interface laws for shear tests of FRP plates bonded to concrete, Composites Part B: Engineering 54 (2013) 329–342.

[9] K. Subramaniam, C. Carloni, L. Nobile, Width effect in the interface fracture during shear debonding of FRP sheets from concrete, Engineering Fracture Mechanics 74 (2007) 578–594.

[10] K. Subramaniam, C. Carloni, L. Nobile, An understanding of the width effect in FRP-concrete debonding, Strain 47 (2011) 127–137.

[11] J. Chen, W. Pan, Three dimensional stress distribution in FRP-to-concrete bond test specimens, Construction and Building Materials 20 (2006) 46–58.

[12] V. Salomoni, G. Mazzucco, C. Pellegrino, C. Majorana, Three-dimensional modelling of bond behaviour between concrete and FRP reinforcement, Engineering Computations 28 (2011) 5–29.

[13] P. Neto, J. Alfaiate, J. Vinagre, A three-dimensional analysis of CFRP–concrete bond behaviour, Composites Part B: Engineering 59 (2014) 153–165.

[14] N. Moës, J. Dolbow, T. Belytschko, A finite element method for crack growth without remeshing, International Journal for Numerical Methods in Engineering 46 (1999) 131–150.

[15] T. Belytschko, R. Gracie, G. Ventura, A review of extended/generalized finite element methods for material modeling, Modelling and Simulation in Material Science and Engineering 17 (2009) 043001.

[16] S. Osher, J. Sethian, Fronts propagating with curvature dependent speed: Algorithms based on a Hamilton-Jacobi formulation, Journal of Computational Physics 79 (1988) 12–49.

[17] D. Mollenhauer, L. Ward, E. Iarve, S. Putthanarat, K. Hoos, SH., X. Li, Simulation of discrete damage in composite overheight compact tension specimens, Composites Part A: Applied Science and Manufacturing 43 (2012) 1667–1679.

[18] Y. Wang, H. Waisman, Progressive delamination analysis of composite materials using XFEM and a discrete damage zone model, Computational Mechanics 55 (2015) 1–26.

[19] F. V. D. Meer, L. Sluys, S. Hallett, M. Wisnom, Computational modeling of complex failure mechanisms in laminates, Journal of Composite Materials 46 (5) (2012) 603–623.

[20] E. Benvenuti, O. Vitarelli, A. Tralli, Delamination of FRP-reinforced concrete by means of an extended finite element formulation, Composites Part B: Engineering 43 (2012) 3258–3269.

[21] E. Benvenuti, A. Tralli, Simulation of finite-width process zone for concrete-like materials, Computational Mechanics 50 (2012) 479–497.

	XFEM	Regularized XFEM
discontinuity	strong	weak
cohesive zone	traction-separation law	regularized stress-strain law
$\mathbf{K}^e$	$\mathbf{K}^e_{st}$ (5)	$\mathbf{K}^e_{reg}$ (6)
quadrature	sub-element quadrature	Gauss quadrature
internal length	no	yes

Table 1: Differences between the proposed approach and Belytschko's et al. [14] original approach; matrix $\mathbf{B}_e$ collects all the elemental contributions and $\mathbf{K}^e$ is the elemental stiffness

[22] E. Benvenuti, Mesh-size-objective XFEM for regularized continuous-discontinuous transition, Finite Elements in Analysis and Design 47 (2011) 1326–1336.

[23] C. Comi, S. Mariani, U. Perego, An extended FE strategy for transition from continuum damage to mode i cohesive crack propagation, International Journal for Numerical and Analytical Methods in Geomechanics 31 (2007) 213–238.

[24] J. Toti, S. Marfia, E. Sacco, Coupled body-interface nonlocal damage model for FRP detachment, Computer Methods in Applied Mechanics Engineering 260 (2013) 1–23.

[25] K. Benzarti, F. Freddi, F. Frémond, A damage model to predict the durability of bonded assemblies. part i: Debonding behaviour of FRP strengthened concrete structures, Construction and Building Materials 25 (2011) 547–555.

[26] MJ. Chajes, WW. Finch Jr, TF. Januszka, TA. Thomson Jr, Bond and force transfer of composite material plates bonded to concrete, ACI Structural Journal 93 (1996) 209–217.

[27] E. Benvenuti, XFEM with equivalent eigenstrain for matrixinclusion interfaces, Computational Mechanics 53 (2014) 893-908.

[28] E. Benvenuti, G. Ventura, N. Ponara, A. Tralli, Variationally consistent extended FE model for 3D planar and curved imperfect interfaces, Computer Methods in Applied Mechanics Engineering 267 (2013) 434–457.

[29] Z. Bažant, P. Pfeiffer, Shear fracture tests of concrete, Matériaux et Constructions 19 (1986) 111–121.

[30] R. Ballarini, A. Franco, G. Royer-Carfagni, Wedge-shaped fracturing in the pull out of FRP stiffeners from quasi-brittle substrates, International Journal of Solids and Structures 51 (2014) 3196–3208.

[31] C. Carloni, KV. Subramaniam, Direct Determination of Cohesive Stress Transfer during Debonding of FRP from Concrete. Composite Structures, 93 (2010) 184–192

[32] Advisory Committee on Technical Recommendations for Construction of National Research Council CNR-DT 200/2004 materials, RC and PC structures, masonry structures Rome, Italy, Guide for the design and construction of externally bonded FRP systems for strengthening existing structures (2004).

	Chajes et al.[26]			Carrara et al. [6]		
	FRP	glue	concrete	FRP	glue	concrete
E [MPa]	108380	1585	33640	168500	3517.3	28700
ν	0.248	0.315	0.2	0.248	0.315	0.2
f_t[MPa]	–	–	3.21	–	–	2.85
thickness [mm]	1.0	1.0	–	1.3	1.3	–
H [mm]	152.4	152.4	152.4	90	90	90
B [mm]	150	150	150	152.4	152.4	152.4
L [mm]	300	300	300	228.6	228.6	228.6
b [mm]	25.4	25.4	25.4	30	30	30

Table 2: Material and geometry parameters

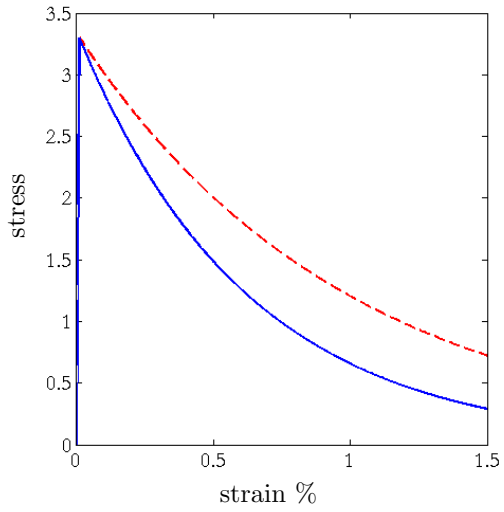

Figure 1:

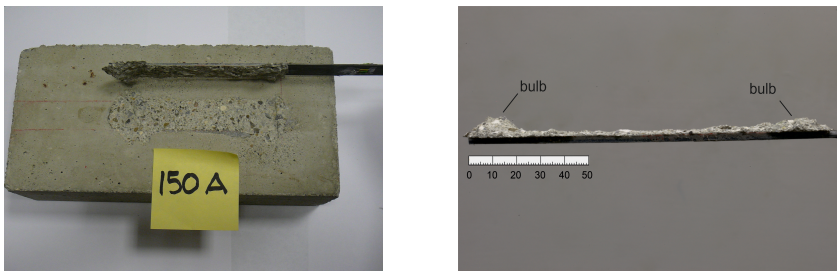

Figure 2:

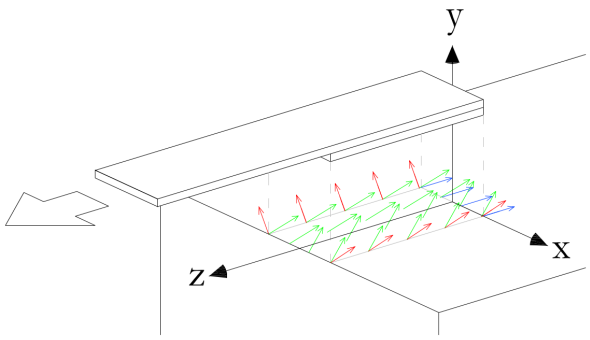

Figure 3:

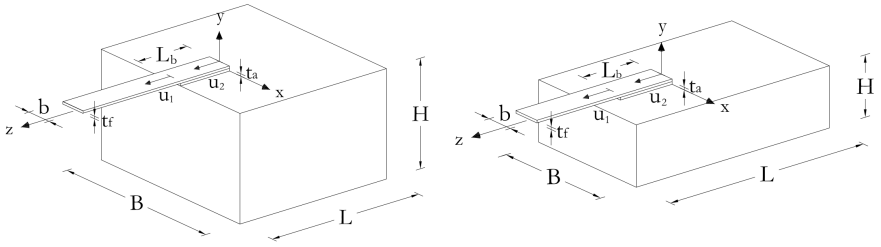

Figure 4:

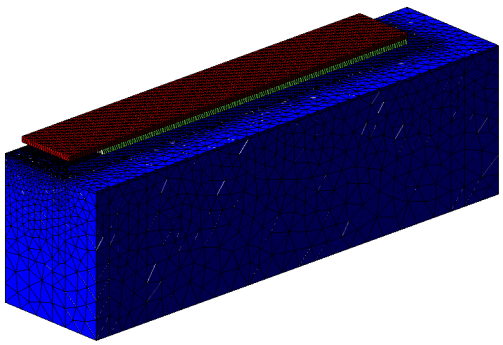

Figure 5:

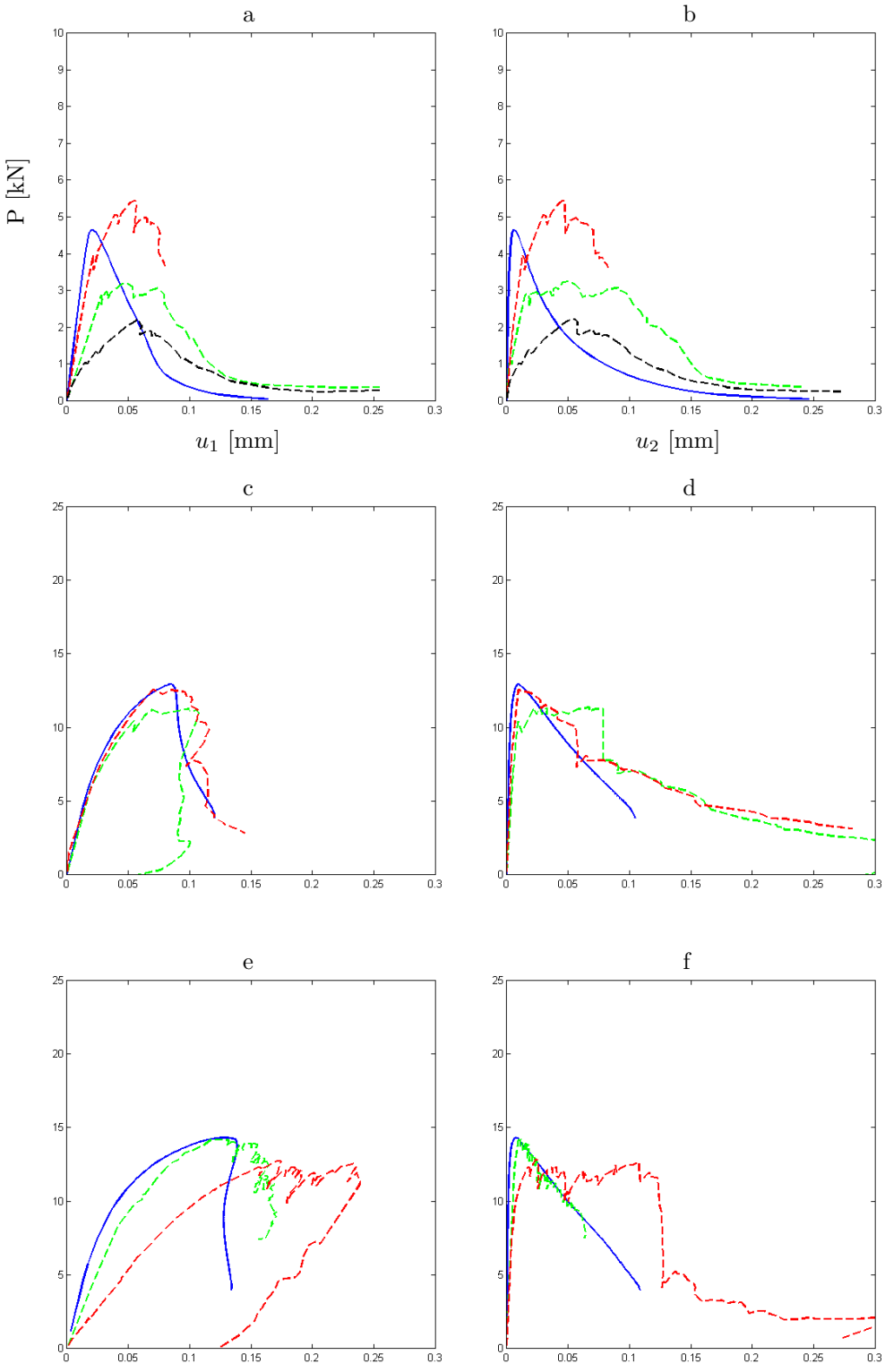

Figure 6:

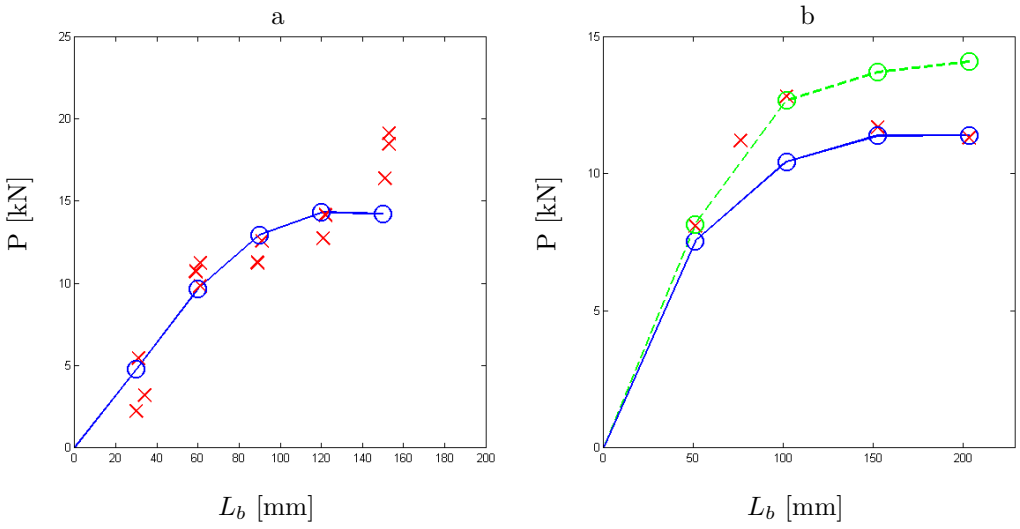

Figure 7:

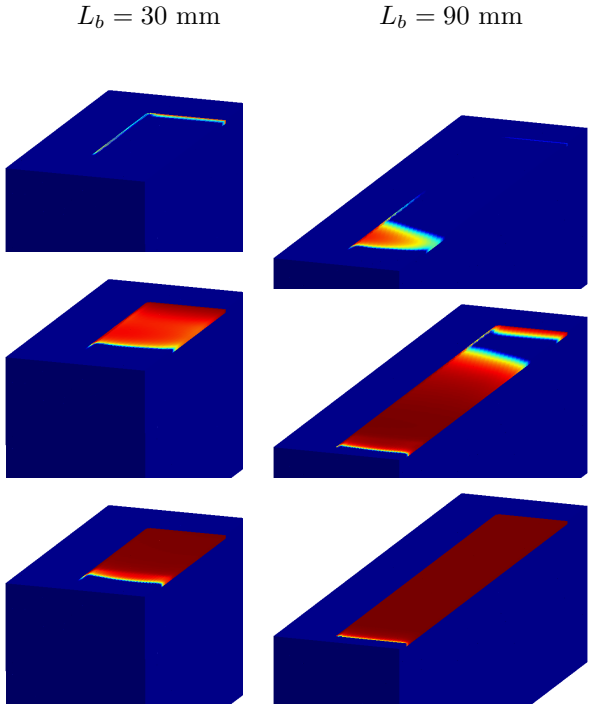

Figure 8:

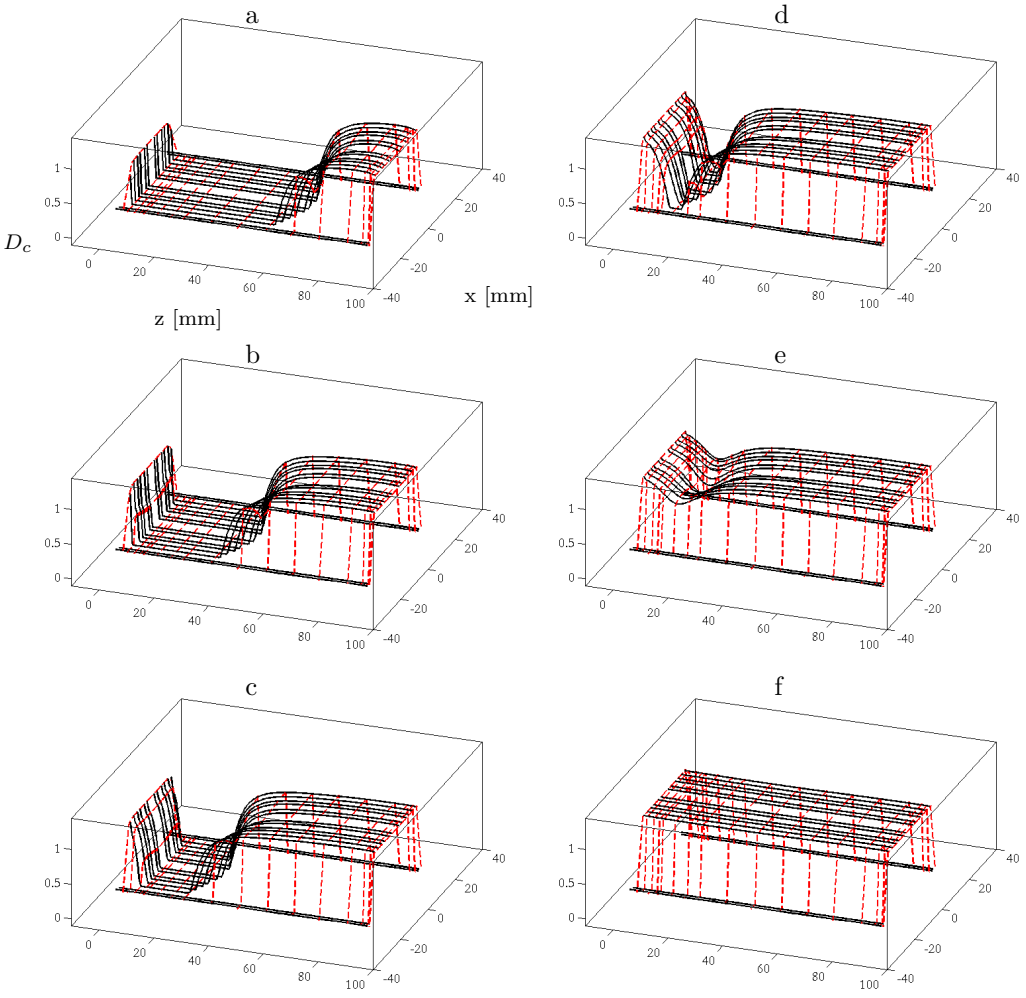

Figure 9:

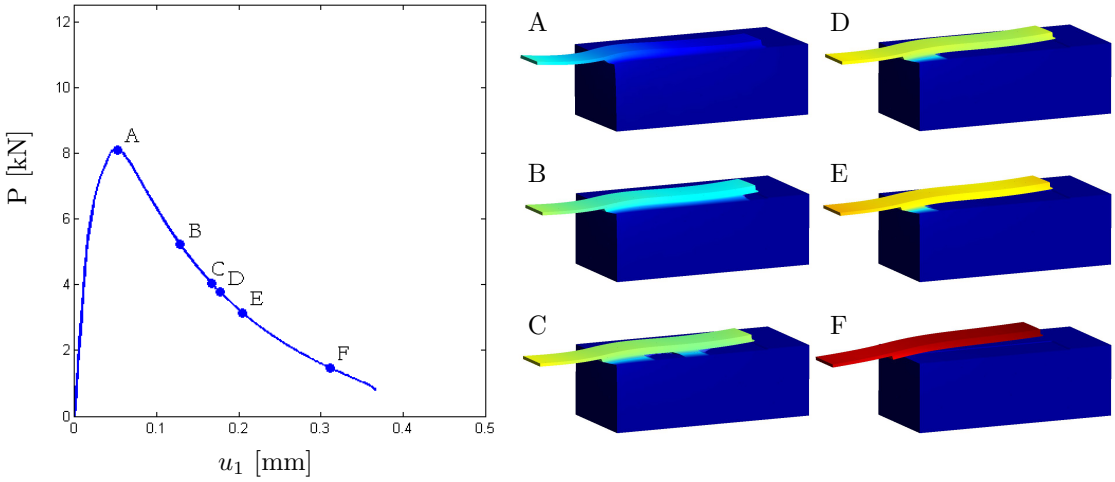

Figure 10:

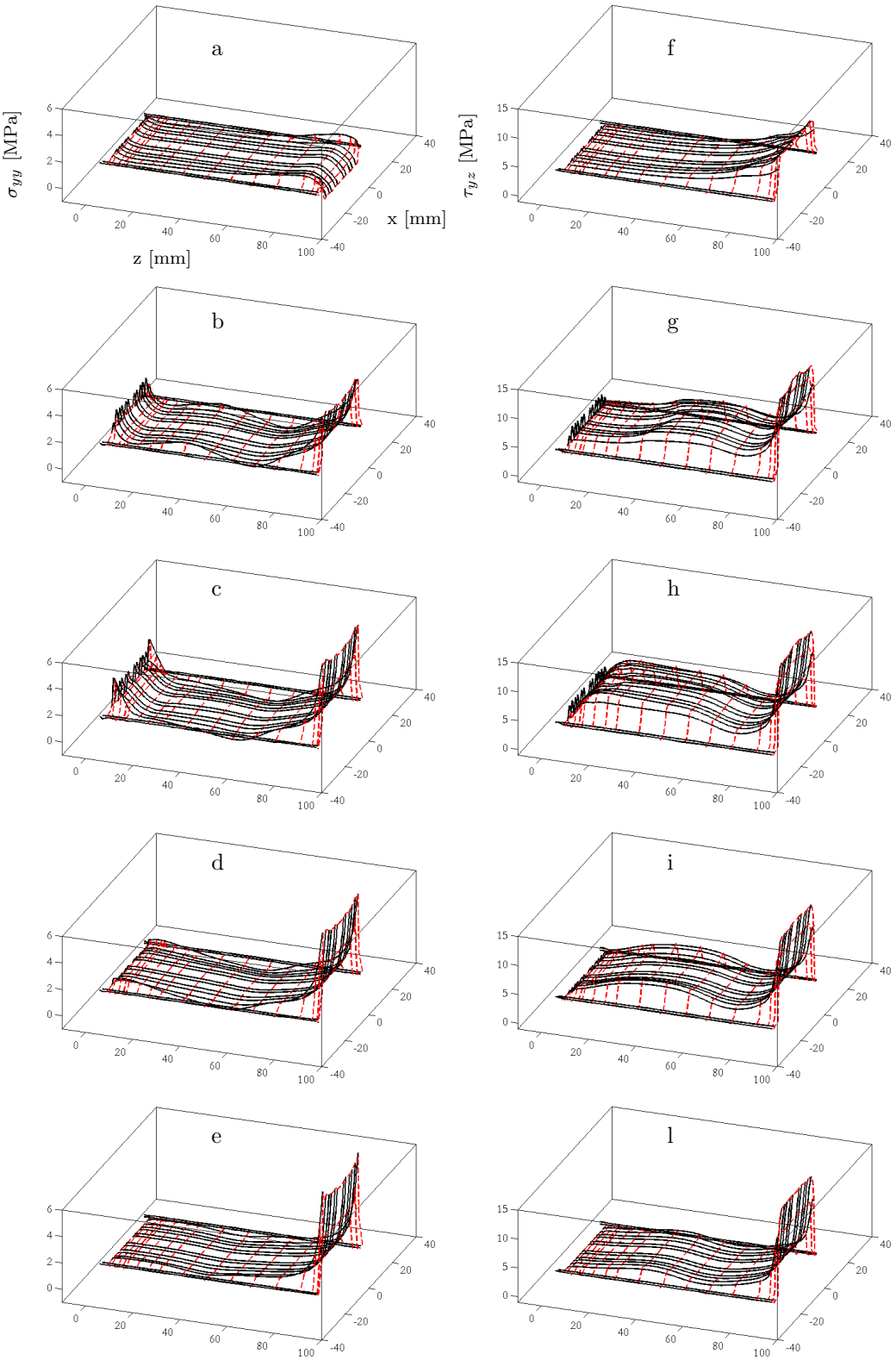

Figure 11:

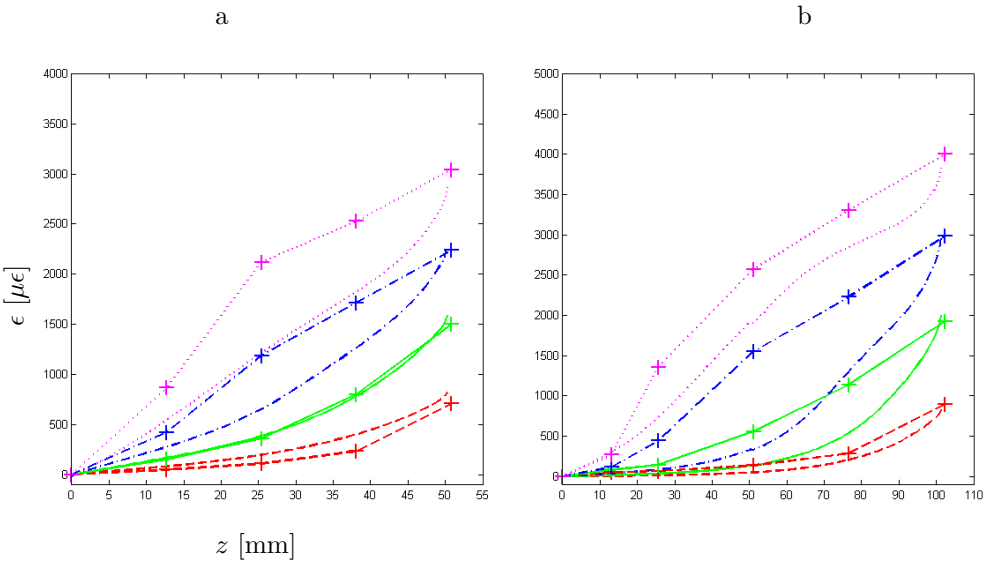

Figure 12:

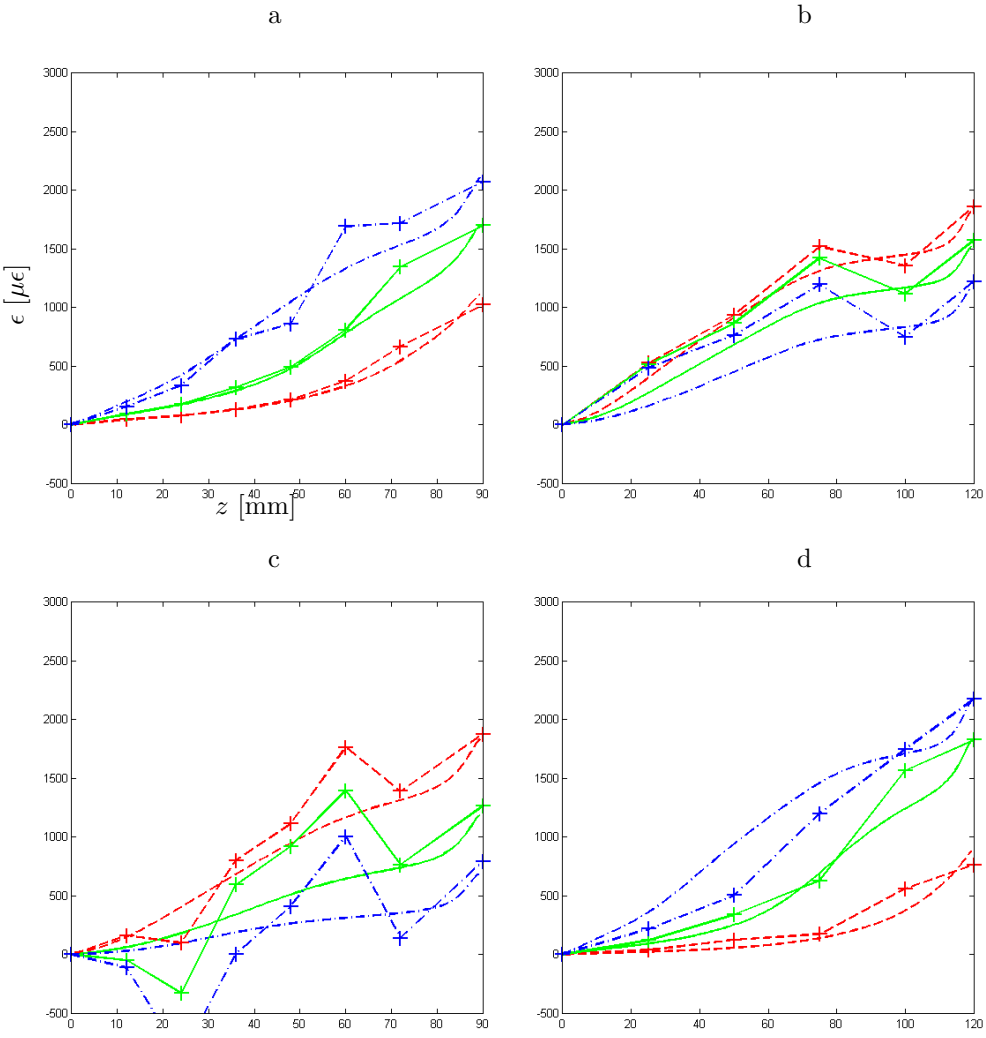

Figure 13:

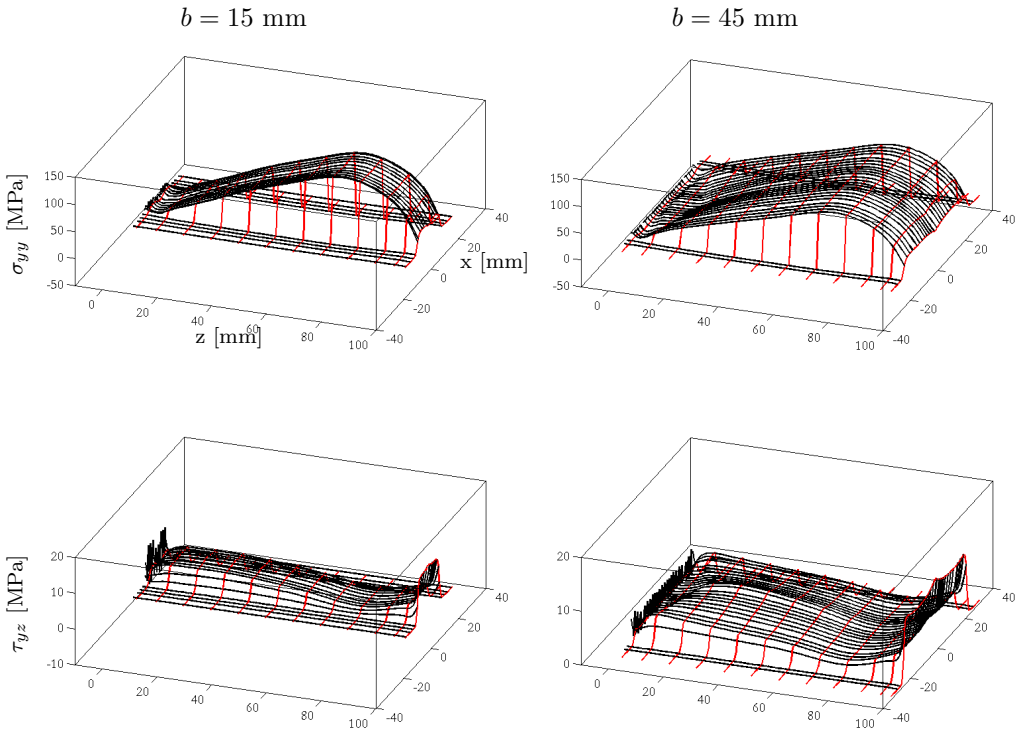

Figure 14:

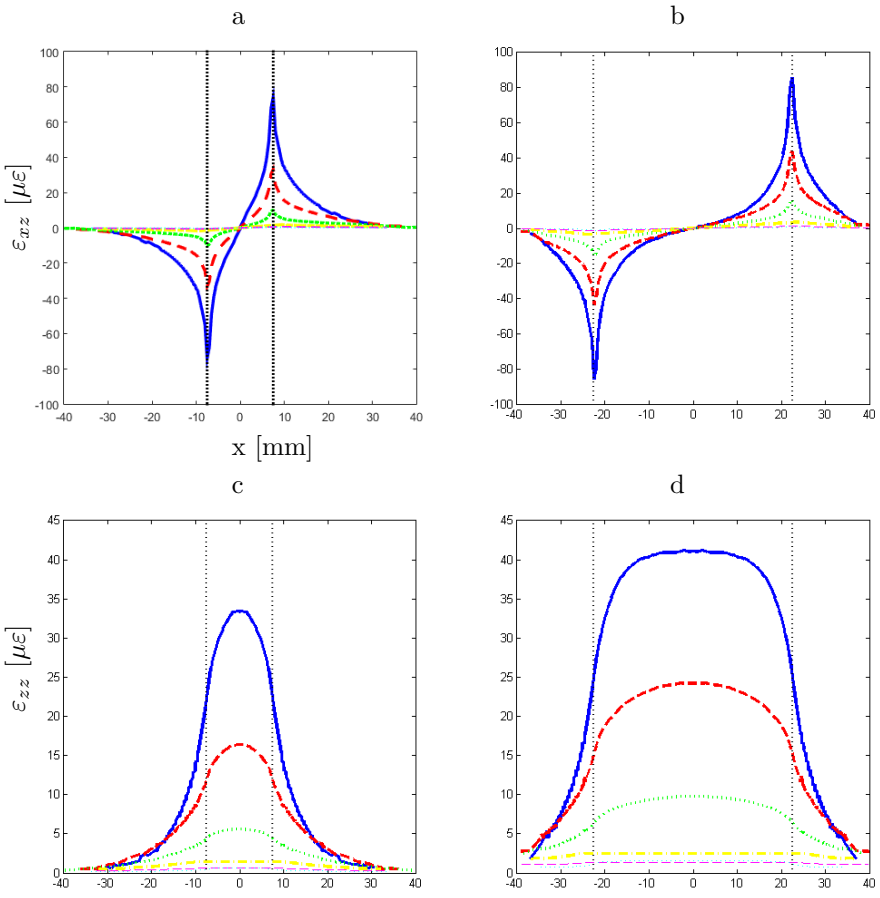
a
b
c
d
ε_{xz} [$\mu\varepsilon$]
ε_{zz} [$\mu\varepsilon$]
x [mm]

Figure 15:

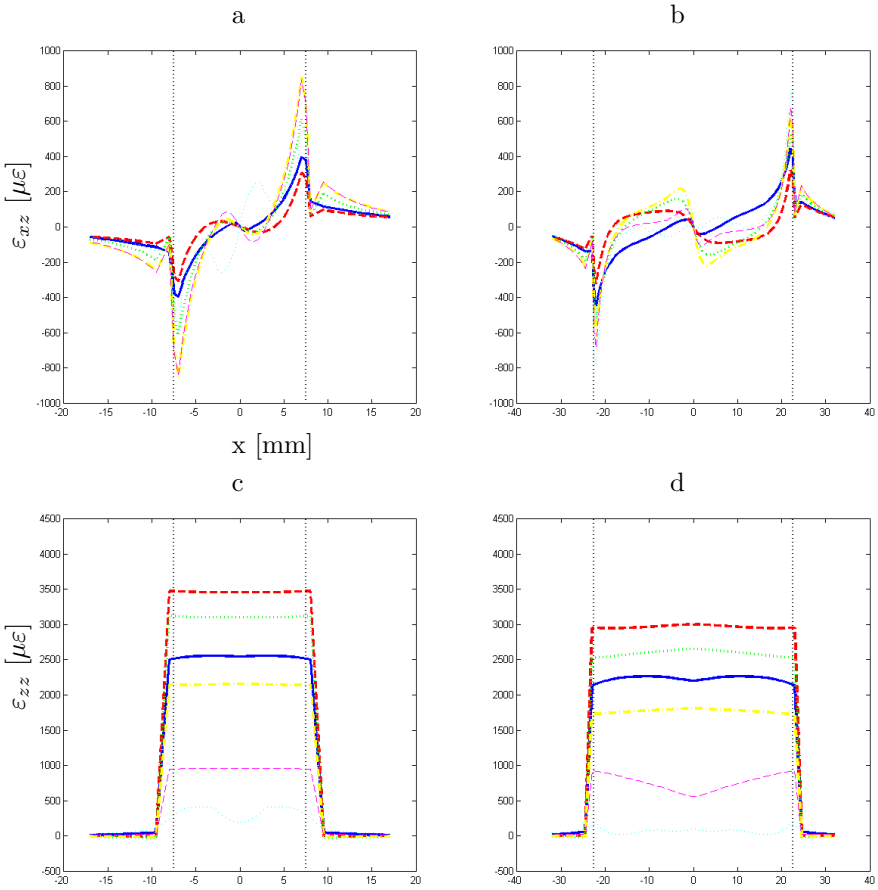
a
b
ε_{xz} [$\mu\varepsilon$]
x [mm]
c
d
ε_{zz} [$\mu\varepsilon$]

Figure 16:

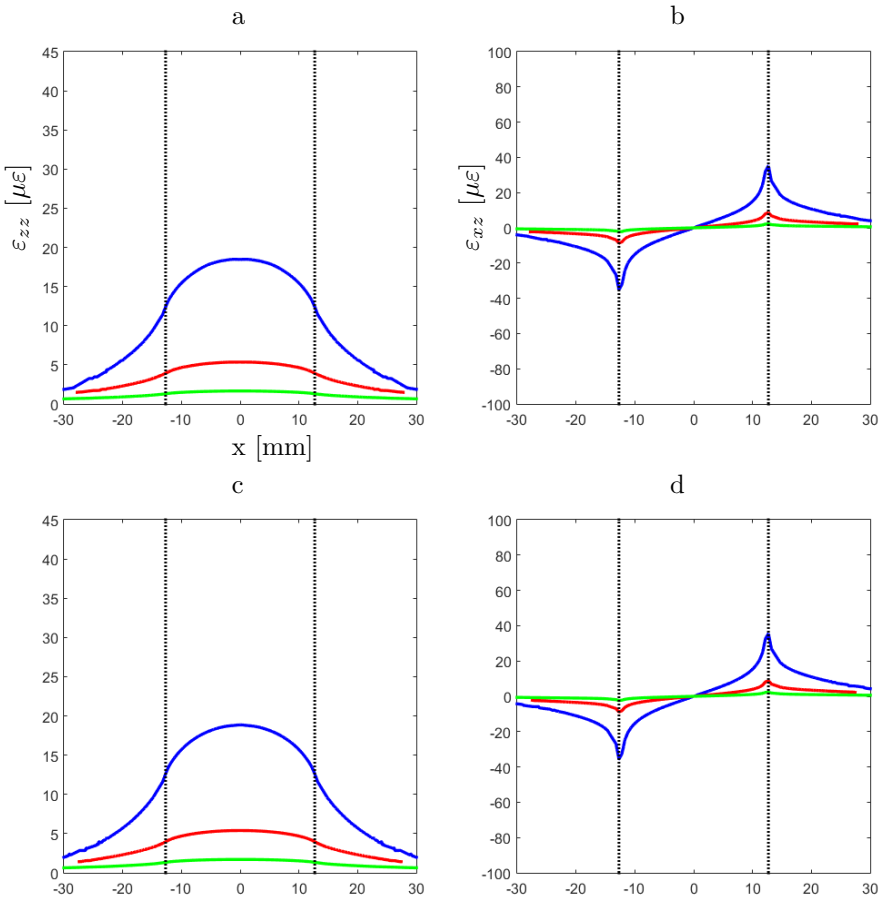
a
b
c
d
ε_{zz} [$\mu\varepsilon$]
ε_{xz} [$\mu\varepsilon$]
x [mm]

Figure 17:

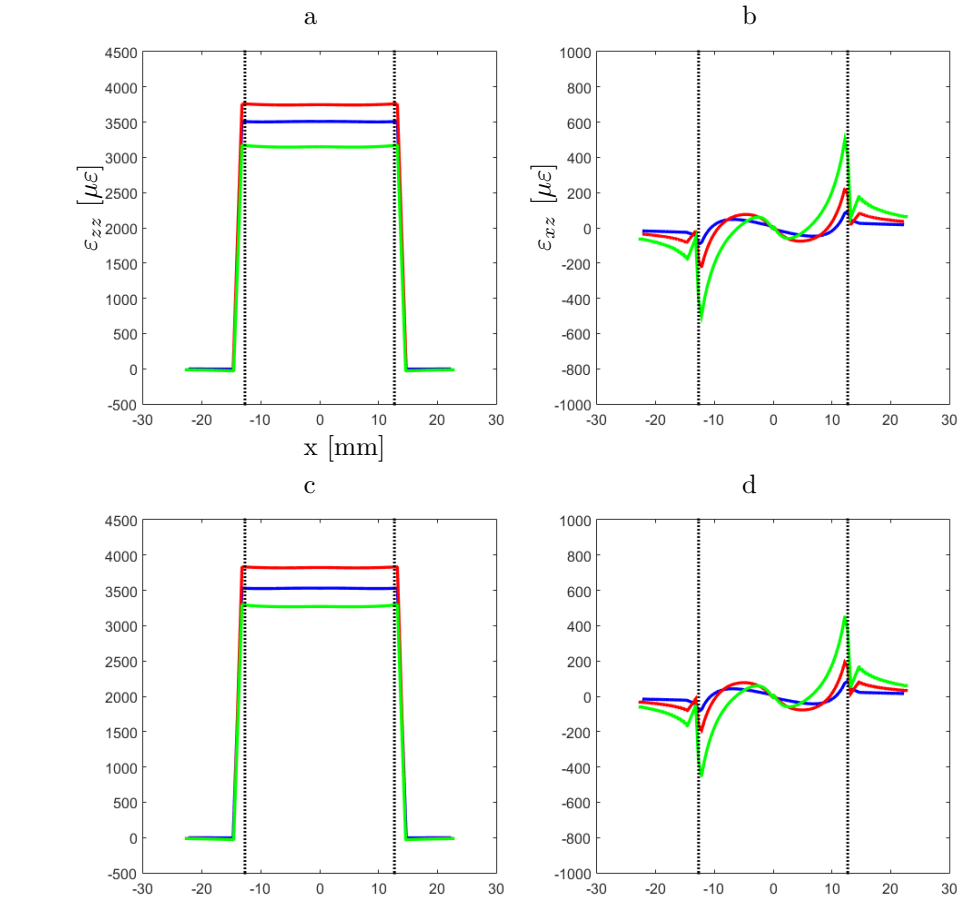

Figure 18:

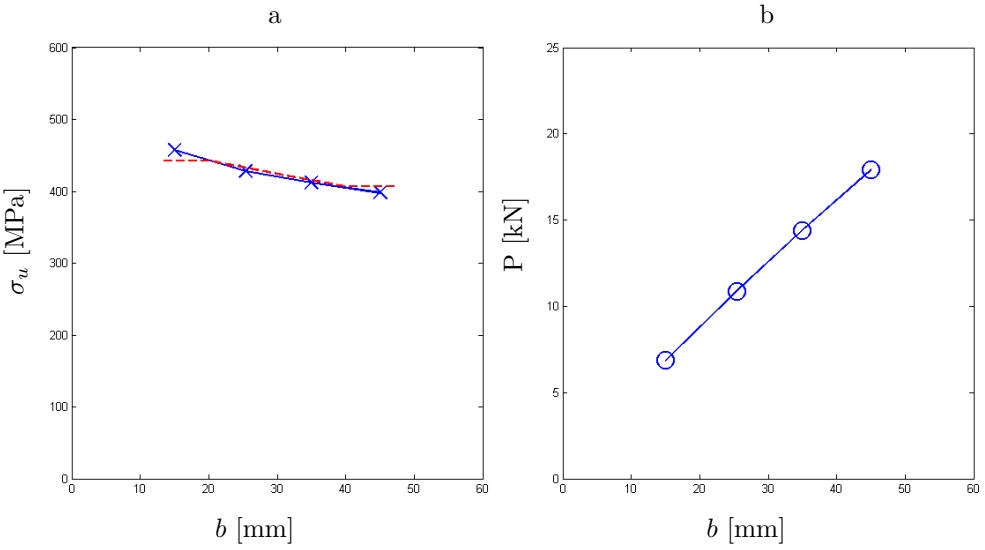

Figure 19:

Figures captions

Fig.1 Stress strain law corresponding to $H = 0.008$ (blue continuous line) and $H = 0.005$ (red dotted line) and $f_t = 3.21$ MPa

Fig.2 Photographs of the detached concrete layer after delamination for the tests of Carrara et al. [6]

Fig.3 Qualitative picture of the vector $\mathbf{n}$ associated with the *local* level set adopted in Eq. (3b)

Fig.4 Geometry of the Chajes et al. [26] (a) and Carrara et al. [6] (b) specimens

Fig.5 Mesh of half of the Chajes et al. [26] specimen

Fig.6 Computed (continuous line) and experimental [6] (dashed lines) load-displacement profiles for $L_b = 30$ mm (a, b), $L_b = 90$ mm (c, d), and $L_b = 120$ mm (e, f) at the loaded and the free end (see Fig. 4)

Fig.7 Computed ("o") and experimental maximum loads ("x") vs bonding length L_b [mm] for the tests [6] a) and [26] b), where the dashed and the continuous lines refer to $H = 0.005$ and $H = 0.008$, respectively

Fig.8 Damage evolution for the test [6] with $L_b = 30$ mm, on the left, and $L_b = 90$ mm, on the right, evaluated (from top to bottom) at $P = 2.60$ kN, $P = 4.76$ kN, and $P = 3.75$ kN

Fig.9 Pre-peak (a,b,c), peak (d) and post-peak (e,f) damage profiles for $L_b = 90$ mm for the test [6]

Fig.10 Computed load-displacement profile for $L_b = 50.8$ mm and corresponding deformed mesh evolution at the loads A, B, C, D, E, F for the test [26]

Fig.11 Pre-peak (a), peak (b) and post-peak (c) profiles of σ_{yy} MPa (peeling) on the left and τ_{yz} MPa (on the right) for the test [6] with $L_b = 90$ mm

Fig.12 1D equivalent axial strain along z for the test [26] obtained for $L_b = 50.8$ mm (a) and $L_b = 101.6$ mm (b). The load levels are: $P = 1.94$ kN (red dashed line), $P = 4.06$ kN (green continuous line), $P = 6.01$ kN (blue dash dotted line line), $P = 8.10$ kN (pink dotted line) (a), and $P = 2.23$ kN (red dashed line), $P = 5.03$ kN (green continuous line), $P = 7.71$ kN (blue dash dotted line line), $P = 10.29$ kN (pink dotted line) (b)

Fig.13 1D equivalent axial strain along z for the test [6] for $L_b = 90$ mm (c) and $L_b = 120$ mm (d), at $P = 6.00$ kN (red dashed line), $P = 10.01$ kN (green continuous line), $P = 12.64$ kN (blue dash dotted line line) in (c), and $P = 5.01$ kN (red dashed line), $P = 12.00$ kN (green continuous line), $P = 14.28$ kN (blue dash dotted line line) (d); $P = 11.15$ kN (red dashed line), $P = 7.47$ kN (green continuous line), $P = 4.67$ kN (blue dash dotted line line) in (e), and $P = 12.21$ kN (red dashed line), $P = 10.33$ kN (green continuous line), $P = 8.04$ kN (blue dash dotted line line) in (f)

Fig.14 3D view of σ_{yy} and τ_{yz} for $b = 15$ mm and $b = 45$ mm with $L_b = 101.6$ mm evaluated at the maximum load for the test [26]

Fig.15 Front view of ε_{xz} (a) and ε_{zz} (b) along x during the elastic stage for $b = 15$ mm (on the left) and $b = 45$ mm (on the right) at $z = 0.5$ mm (cyan dotted line), $z = 18.1$ mm (pink dashed line), $z = 38.1$ mm (yellow dash-dotted line), $z = 58.1$ mm (green dotted line), $z = 78.1$ mm (red dashed line) and $z = 95.1$ mm (blu continuous line) for the test [26]

Fig.16 Front view of ε_{xz} (a) and ε_{zz} (b) along x at the maximum load for $b = 15$ mm (on the left) and $b = 45$ mm (on the right) in the test [26] (notation as in the previous Figure)

Fig.17 Front view of ε_{zz} (a,c) and ε_{xz} (b,d) along x during the elastic stage for $L_b = 152.4$ mm (on the left) and $L_b = 203.2$ mm (on the right) evaluated at a distance from the front of 25.4 mm (blue line), 50.8 mm (red line), and 76.2 mm (green line) for the test [26]

Fig.18 Front view of ε_{xz} (a,c) and ε_{zz} (b,d) along x at the peak load for $L_b = 152.4$ mm (on the left) and $L_b = 203.2$ mm (on the right) evaluated at a distance from the front of the concrete block of 25.4 mm (blue line), 50.8 mm (red line), and 76.2 mm (green line) for the test [26]

Fig.19 Computed nominal stress (a) and maximum load (b) vs bond width b and the CNR-design-rule (7) with $\kappa_g = 0.065$ (dashed line) for the test [26]